Canary Current and North Equatorial Current from an inverse box model

Alonso Hernández-Guerra,[1] Eugenio Fraile-Nuez,[1] Federico López-Laatzen,[2] Antonio Martínez,[1] Gregorio Parrilla,[3] and Pedro Vélez-Belchí[2]

Received 28 April 2005; revised 14 July 2005; accepted 17 August 2005; published 20 December 2005.

[1] The large-scale Canary Basin circulation is estimated from a box inverse model applied to hydrographic data from a quasi-synoptic survey carried out in September 2003. The cruise consisted of 76 full depth CTD and oxygen stations. Circulation is required to nearly conserve mass and anomalies of salinity and heat within layers bounded by neutral surfaces. It permits advective and diffusive exchange between layers and an adjustment of the Ekman transport and the freshwater flux divergences. The Canary Current at the thermocline layer transports a net mass of 4.7 ± 0.8 Sv southward north of the Canary Islands from the African coast to 19°W. It is divided into a northward circulation at a rate of 1.1 ± 0.5 Sv between the African coast and Lanzarote Island and a southward transport of 5.8 ± 0.6 Sv. It transports North Atlantic Central Water and organic matters advected offshore by the filaments protruding from the upwelling system off northwest Africa. At 24°N, the Canary Current feeds the North Equatorial Current that transports a mixture of North and South Atlantic Central Waters westward. In the intermediate layer a southwestward flow of 1.2 ± 1.1 Sv transports Mediterranean Water to the Subtropical Gyre, though the highest salt flux is transported by a meddy. Oxygen distribution and mass transport suggest a northeastward deep flow of a water mass colder than 2.2°C consisting of diluted Antarctic Bottom Water. The heat and freshwater divergences and the average dianeutral velocity and diffusion between the sections and the African coast are negligible.

Citation: Hernández-Guerra, A., E. Fraile-Nuez, F. López-Laatzen, A. Martínez, G. Parrilla, and P. Vélez-Belchí (2005), Canary Current and North Equatorial Current from an inverse box model, *J. Geophys. Res.*, *110*, C12019, doi:10.1029/2005JC003032.

1. Introduction

[2] The Canary Current and the North Equatorial Current are surface currents that define the eastern and southern dynamic boundaries of the North Atlantic Subtropical Gyre. During the 1980s, the eastern basin of the North Atlantic Subtropical Gyre was studied in depth, although the majority of the sampling was done at the northern boundary, the Azores Current [*Käse and Siedler*, 1982; *Gould*, 1985; *Sy*, 1988; *Klein and Siedler*, 1989; *Stramma and Müller*, 1989; *Fiekas et al.*, 1992; *Arhan et al.*, 1994]. The Canary Current and the North Equatorial Current were mainly studied using historical data [*Stramma*, 1984; *Stramma and Siedler*, 1988; *Stramma and Isemer*, 1988]. The Azores Current flows eastward south of the Azores Archipelago, it turns south in three main branches, the most easterly one, east of Madeira Island, feeds the Canary Current. This current flows southwestward along the African coast, turning west into the open ocean at approximately 20°–25°N where it joins the North Equatorial Current. *Stramma and Müller* [1989] found that the North Equatorial Current flows north of the Cape Verde Frontal Zone (CVFZ) that separates the North Atlantic Central Water (NACW) from the South Atlantic Central Water (SACW) [*Barton*, 1987; *Zenk et al.*, 1991]. Surface currents do not cross south of the CVFZ, which represents the boundary between the ventilated subtropical gyre and what has been called the shadow zone [*Luyten et al.*, 1983; *Cox and Bryan*, 1984].

[3] At the end of the 1990s, under the auspices of the European Union funded project CANIGO (Canary Islands Azores Gibraltar Observations) newly collected data allowed further study of the Canary Current north of the Canary Islands [*Parrilla et al.*, 2002]. During the span of this project, four cruises were staged between Madeira and the Canary Islands, each in a different season [*Knoll et al.*, 2002]. F. Machín et al. (Mass and nutrient seasonal fluxes by the Canary Current as determined with inverse methods, submitted to *Progress in Oceanography*, 2005, hereinafter referred to as Machín et al., submitted manuscript, 2005) applied an inverse box model to the hydrographic data collected from these four cruises and obtained the average and seasonal circulation of the Canary Current north of the Canary Islands. The average Canary Current consists of a southwestward mass transport of 3.0 ± 1.0 Sv (1 Sv =

[1]Facultad de Ciencias del Mar, Universidad de Las Palmas de Gran Canaria, Las Palmas, Spain.
[2]Centro Oceanográfico de Canarias, Instituto Español de Oceanografía, Santa Cruz, Spain.
[3]Intituto Español de Oceanografía, Madrid, Spain.

0148-0227/05/2005JC003032

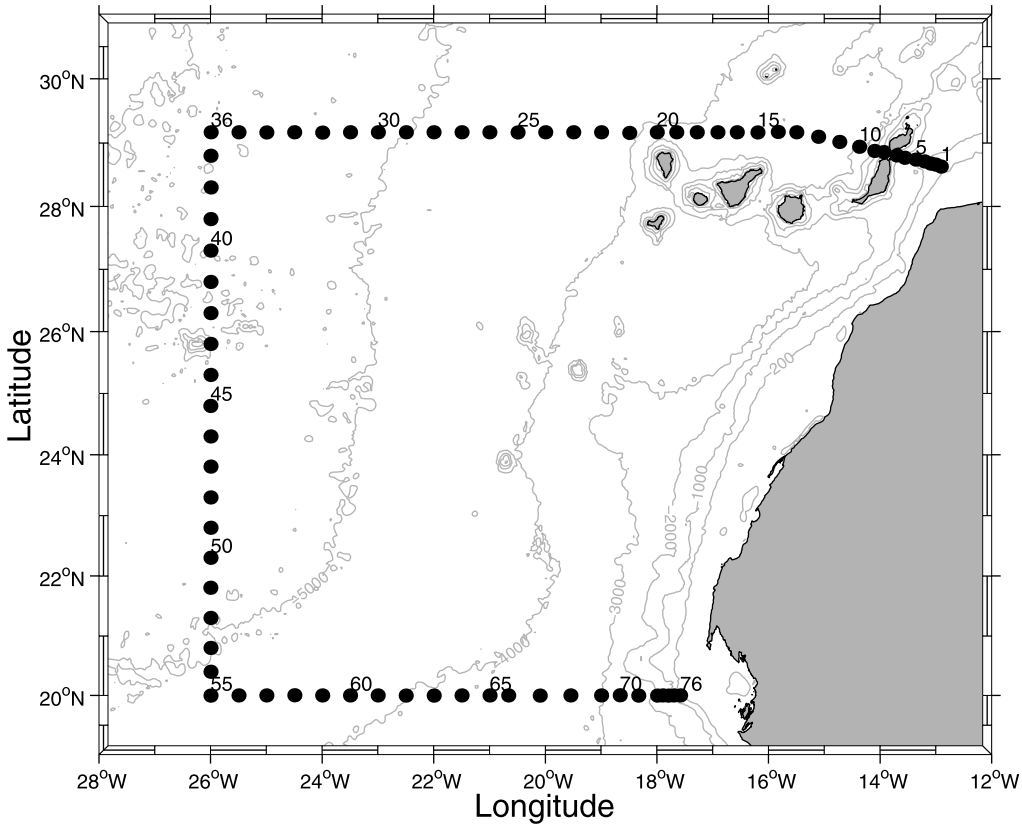

Figure 1. Location of the CTD stations shown (solid dots). For reference, the 200, 1000, 2000, 3000, 4000, and 5000 m isobaths are shown [*Smith and Sandwell*, 1997].

10^6 m^3 s^{-1} $\sim$ 10^9 kg s^{-1}) and a second branch of 1.0 ± 0.3 Sv related to the coastal upwelling off northwest Africa. During the winter, the Canary Current almost disappears in the Canary Islands, and although there is a seasonal spatial shift, transport does not vary significantly in the remaining three seasons. In the spring, the Canary Current flows near the African coast, in summer through the whole Canary Archipelago and in autumn only through the western islands. During the later season, a northward circulation between Lanzarote Island and the African coast develops. This seasonal pattern is also observed in the maps of *Stramma and Siedler* [1988] for the 0–200 m integrated volume transport. The second branch is present in spring and summer, when the Trade winds intensify, favoring the coastal upwelling [*Wooster et al.*, 1976; *Speth and Detlefsen*, 1982; *Nykjaer and Van Camp*, 1994]. During September, the trade winds weaken over the Canary Islands and typify the autumn season. Machín et al. (submitted manuscript, 2005) also concluded that the mass transport at intermediate and deep layers in the average cruise is not significantly different than zero.

[4] The main purpose of our study is to determine the mass transport in the water column south of the Canary Islands, in the Canary Current and the North Equatorial Current regions, and to discuss them in terms of water masses. Mass transport is estimated using an inverse method that provides a solution within dynamically consistent error bars. After a brief presentation, in section 2, of the collected hydrographic data, we will describe in section 3 the different water masses using potential temperature/salinity diagrams and vertical sections of potential temperature, salinity, neutral density and oxygen. In section 4 the geostrophic mass transport calculations are presented. In section 5 the inverse box model and its results are described, including heat and freshwater fluxes. In section 6 the adjusted mass transport in terms of water masses is presented and our final discussion is given in section 7.

2. Data

[5] The CORICA cruise occurred between 7 and 29 September 2003 aboard the R/V Thalassa. It consisted of 76 SeaBird 911+ CTD stations taken along three sections that form a box with the African coast (Figure 1). Data were acquired at each station from the surface down to 10–50 m above the bottom. The first section ran due west at 29°10'N from the African coast to 26°W. The second section ran meridionally southward to 20°N, and the third section zonally toward the African coast. Distance intervals between stations were approximately 50 km except for the African slope stations which were 10 km apart.

[6] Water samples were collected at each station with a 24–10 L bottles carousel. The CTD was equipped with a redundant temperature and salinity sensor for intercomparison during the cruise. Temperature and pressure sensors were calibrated at the SeaBird laboratory before the cruise. On board salinity calibration was carried out with a Guildline AUTOSAL model 8400 B salinometer with a precision better than 0.002 for single samples. In situ precision comparisons using six samples from the same bottle and

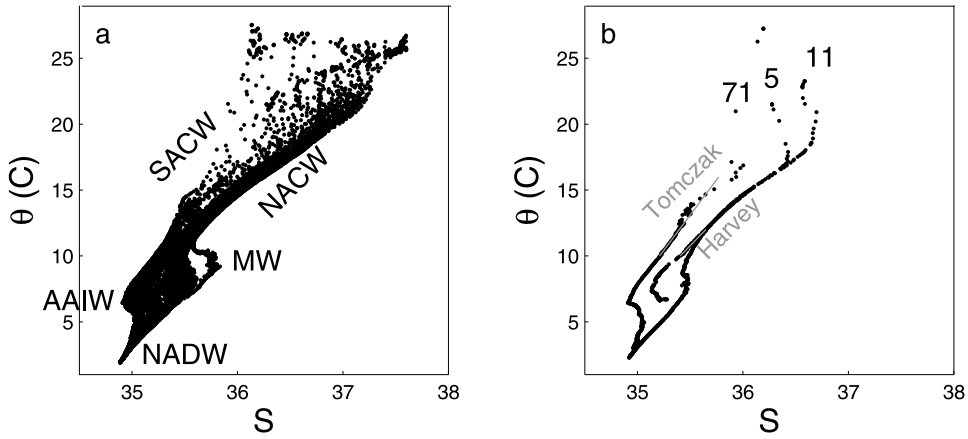

Figure 2. Potential temperature/salinity diagram for (a) all stations and (b) stations 5, 11 m and 71. For comparison, straight lines proposed by *Harvey* [1982] and *Tomczak and Hughes* [1980] as the θ/S relationships for NACW and SACW, respectively, are shown.

six samples from different bottles at the same depth (3478 m, station 17) were 0.007 and 0.005, respectively.

[7] Water sample dissolved oxygen was analyzed by the Winkler method. The precision of the measurements was determined using 6 bottles in station 39 at 800 m and 5000 m depth corresponding to an dissolved oxygen minimum and maximum, respectively. The results give a precision of 0.45% and 0.2% for each depth. Because of instrument problems, no dissolved oxygen data were obtained at stations 1 and 38.

3. Water Masses

[8] To identify water masses and their associated spatial and density/depth distribution potential temperature/salinity diagrams and vertical sections of potential temperature, salinity, neutral density (γ_n) and dissolved oxygen are shown (Figures 2–6). The neutral density algorithm of *Jackett and McDougall* [1997] has been used as the 'density' variable throughout this paper and as a reference level to estimate the geostrophic current. Neutral density values and potential density values are very similar in the upper ocean, and the former can be used in the whole water column to avoid using different potential densities referenced to different depths.

[9] Central waters extend from the surface to a density level of $\gamma_n \sim 27.38$ kg m^{-3} (approximately 700 m depth) defining the surface or thermocline layer. Figure 2 shows that the shallowest layer above the seasonal thermocline (approximately 50 m) presents a scattering of θ/S values due to the seasonal heating, evaporation and eventually cold and low-salinity water advected by upwelling filaments generated in the upwelling area off northwest Africa [*Van Camp et al.*, 1991; *Hernández-Guerra et al.*, 1993; *Nykjaer and Van Camp*, 1994; *Barton et al.*, 1998; *Pacheco and Hernández-Guerra*, 1999]. Figure 3 shows that temperature is generally higher than 24°C and decreases to 22°C toward the African coast in the northern section. Subtropical high-salinity water characterized by the highest salinity (>37.3) due to excessive evaporation is observed in the northwestern corner (Figure 4). Figures 3 and 4 show isotherms and isohalines outcropping.

[10] Below the seasonal thermocline, North Atlantic Central Water (NACW) (Figure 2b, stations 5 and 11) and the less saline South Atlantic Central Water (SACW) (Figure 2b, station 71) are present in the northern and southern sections, respectively [*Emery and Meincke*, 1986]. We have also shown the straight lines (10°C, 35.405)/(10°C, 35.21) and (12°C, 35.65)/(16°C, 35.77) proposed by *Harvey* [1982] and *Tomczak and Hughes* [1980] as the θ-S relationships for NACW and SACW, respectively. It is clear from this plot that the north transect consists of NACW, the south transect mainly of SACW and the western transect of a mixture of SACW and NACW. In the northern section (Figures 3a and 4a) the isolines slope is small, which characterizes the NACW. In the southern section (Figures 3c and 4c) they show a wavelength of approximately 200 km due to the meandering in the boundary between NACW and SACW in the CVFZ [*Barton*, 1987; *Zenk et al.*, 1991; *Fiekas et al.*, 1992; *Pérez-Rodríguez et al.*, 2001]. According to *Barton* [1987] and *Zenk et al.* [1991], the 36.0 isohaline intersecting the 150 m isobath defines the position of the front. Figure 4b shows that the front is located south of 20°N, and west of 21.5°W. A further discussion of the data regarding the frontal region is presented by A. Martínez et al. (Distribution of water masses and currents in the Cape Verde Frontal Zone, manuscript in preparation, 2005). The difference between NACW and SACW stands out even more clearly in the dissolved oxygen distributions (Figure 6). SACW has a lower dissolved oxygen content than NACW. The southern transect shows a patchy distribution of dissolved oxygen that corresponds to the wave structure of isotherms and isohalines. The relative minimum dissolved oxygen (<100 μmole kg^{-1}) is related to the wave crest of the isolines and the relative maximum dissolved oxygen is found in the wave trough due to a mixture of NACW and SACW showing the meandering of the CVFZ. The western transect shows the transition from SACW to NACW. Isotherms and isohalines show a relatively high slope from 20°N to 26°N showing a northward decrease of SACW percentage. The same pattern is also observed in Figure 6b where a northward increase of dissolved oxygen is seen. At 26°N, the 160 μmole kg^{-1} isoline presumably marks the transition between NACW and SACW already mentioned

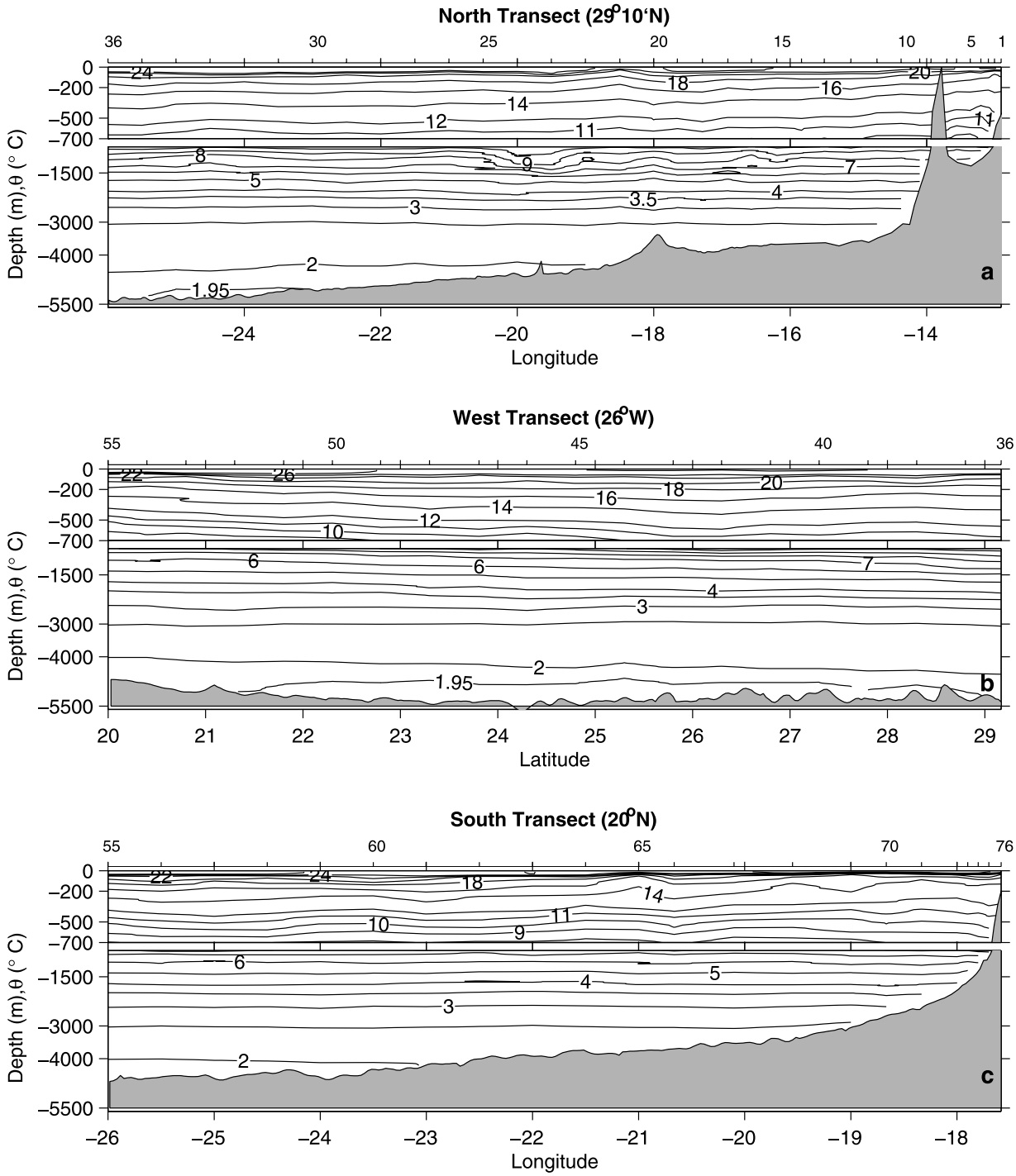

Figure 3. Potential temperature (°C) for the (a) north (western end is on the left), (b) west (northern end is on the left), and (c) south (western end is on the left) sections. Note that the vertical scale changes at 700 m depth. CTD station numbering is indicated in the top axis.

by *Arhan et al.* [1994] as a second front between both water masses.

[11] Below the central waters, the intermediate layers ($27.38 < \gamma_n < 27.922$ kg m^{-3}, roughly 700–1600 m depth) are affected by two water masses, a fresher (<35.1) Antarctic Intermediate Water (AAIW) and a warmer and saltier (>35.4) Mediterranean Water (MW) (Figure 2) [*Worthington*, 1976; *Käse et al.*, 1986; *Arhan et al.*, 1994]. The highest salinity (>35.7) is due to a meddy (Mediterranean Water eddy) in the northern transect at approximately 20°W. The anomalous warm and salty core water of the meddy extends horizontally about 150 km and vertically from around 700 m to 1500 m. As we will see, the dynamical effects of the meddy extend to the thermocline layer. Spatial distribution of AAIW and MW is well defined: the MW signature is stronger in the northern

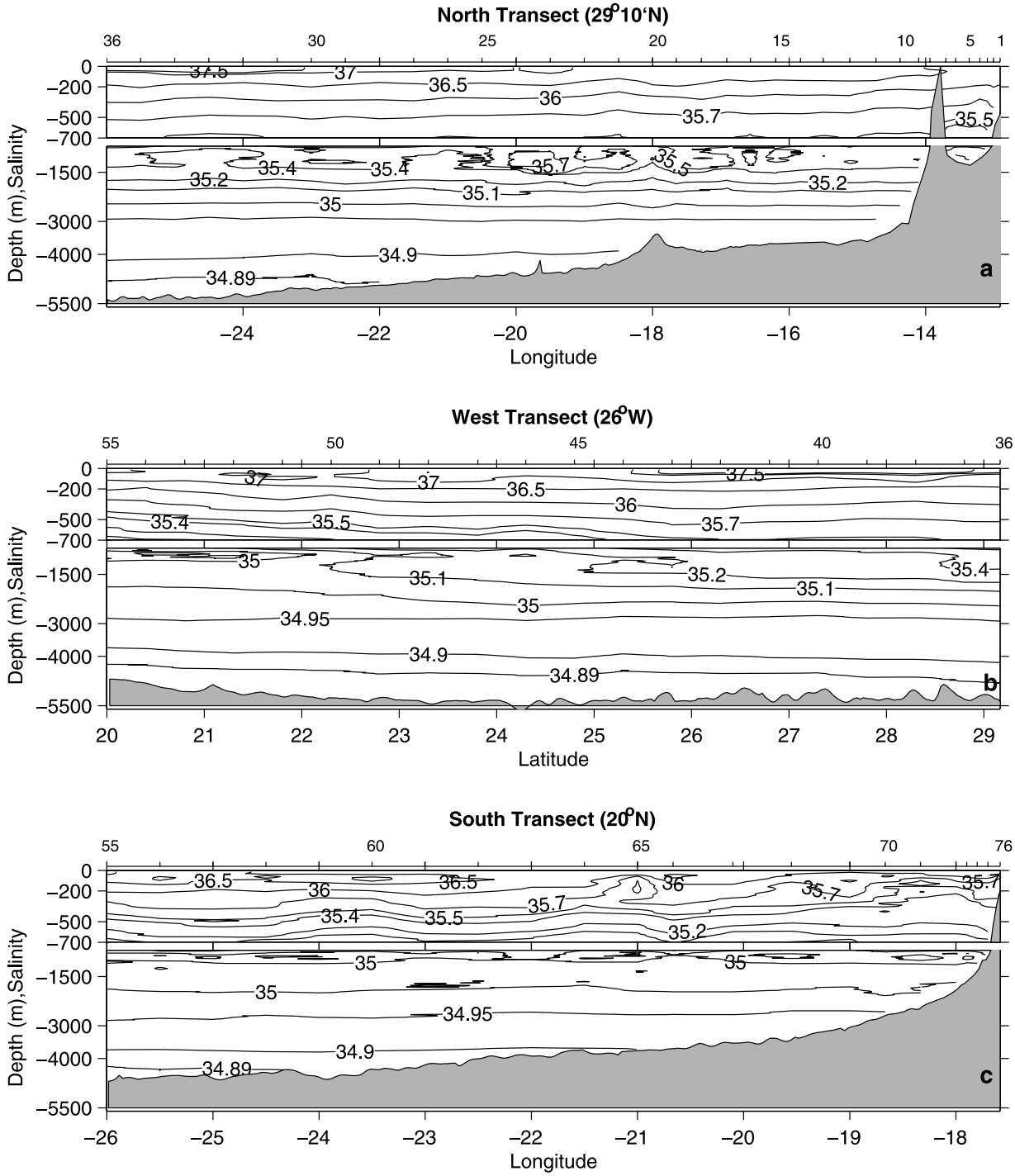

Figure 4. Salinity sections. See Figure 3 caption for details.

section and the AAIW in the southern section (Figures 3a, 3c, 4a, and 4c). In the western section (Figure 4b) there is a gradual northward decrease of AAIW and the transition between AAIW and MW occurs over a wide latitudinal range. The northern transect shows a salinity minimum (<35.2) in the Lanzarote passage clearly seen in the θ/S diagram corresponding to station 5 (Figure 2b) as already described by *Hernández-Guerra et al.* [2001, 2003]. Thus AAIW has a greater influence than SACW in the north. The exact path of AAIW to the Lanzarote passage is still unknown. *Roemmich and Wunsch* [1985] suggested an eastward flow of AAIW in the tropics to feed a northward current along the African coast. *Fratantoni and Richardson* [1999] showed the trajectory of a neutrally buoyant SOFAR float, at depths of 950–1150 m that it was advected northward parallel to, and within ∼150 km of the eastern boundary until near 22°N. *Iorga and Lozier* [1999], using an inverse model to climatological data, showed a northward current along the African coast from 25°N to the Straits of Gibraltar. It seems that the northward

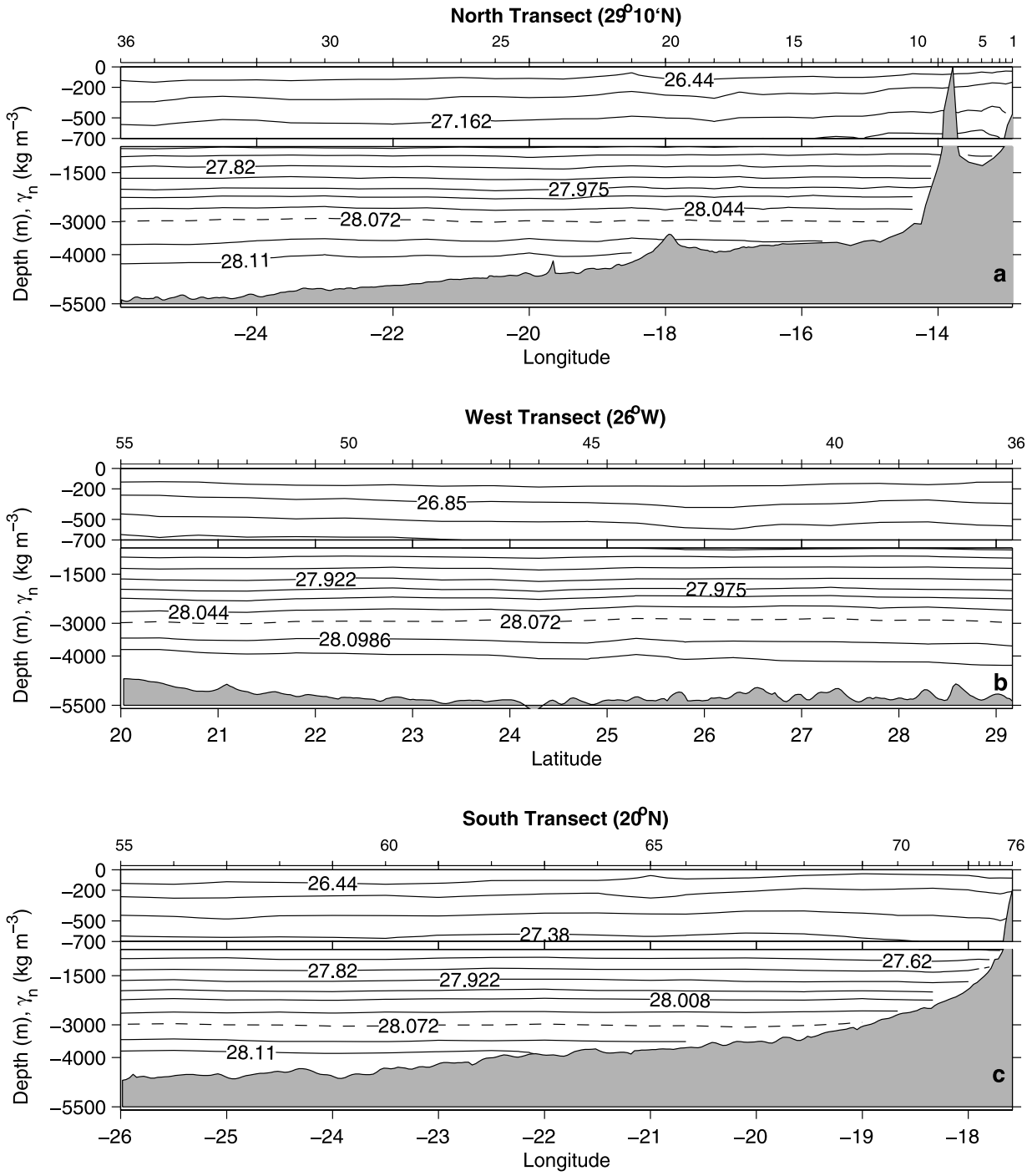

Figure 5. Neutral density sections. See Figure 3 caption for details.

flow transporting AAIW could continue from at least 14°N to the Straits of Gibraltar.

[12] The deep layers from approximately 1600 m to the ocean bottom (γ_n > 27.922 kg m^{-3}) define the North Atlantic Deep Water (NADW). *Wüst* [1935] defined three subclasses of NADW, Upper North Atlantic Deep Water (UNADW), Middle North Atlantic Deep Water (MNADW) and Lower North Atlantic Deep Water (LNADW) on the basis of salinity and oxygen distributions. The shallowest deep water mass is the UNADW identified by a salinity maximum derived from and including MW. Well-developed UNADW appears in the northern section at $\gamma_n \sim 27.975$ kg m^{-3} (roughly 2000 m depth). MW influence decreases southward as it can be seen in the western section. The water mass in the southern section is about 1°C colder and 0.15 less saline than the northern section. Below the salinity maximum there is a water mass of nearly uniform dissolved oxygen (230–240 μmole kg^{-1}) identified as the MNADW. This water mass is thicker east of 18°W and 23°W in the northern and southern transect, respectively, extending down to the bottom. At γ_n > 28.072 kg m^{-3} (roughly 3000 m depth), a large body of water with a deep maximum and

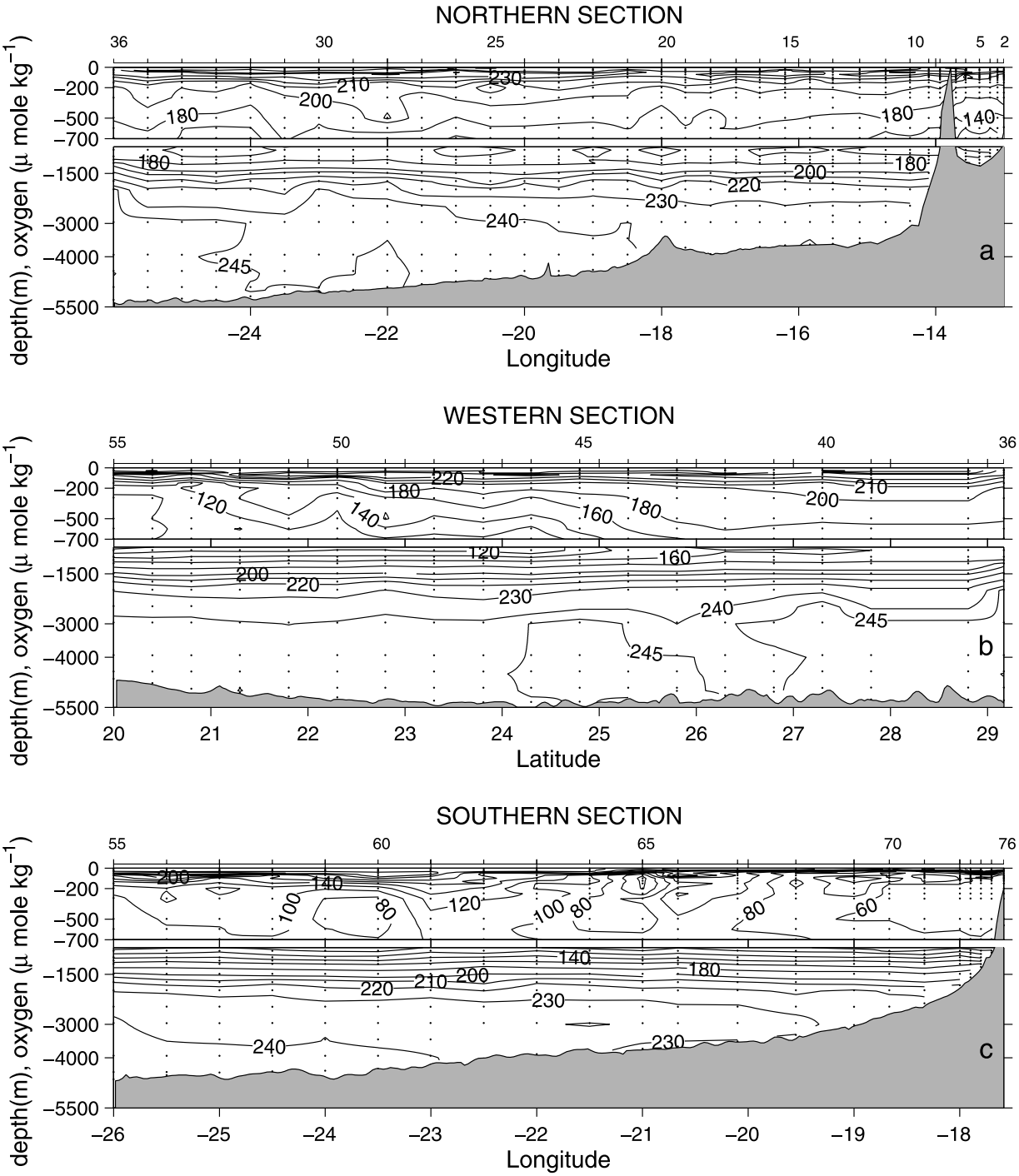

Figure 6. Dissolved oxygen (μmole kg^{-1}) sections. Dots indicate the locations of the sample bottles. See Figure 3 caption for details.

nearly uniform dissolved oxygen (>240 μmole kg^{-1}) is identified as LNADW. According to *Tsuchiya et al.* [1992] the Antarctic Bottom Water (AABW) signal is detected in this basin with its characteristic potential temperature, salinity and dissolved oxygen of approximately 1.95°C, 34.88 and 5.63 mL L^{-1} (roughly 245 μmole kg^{-1}), respectively. Sections of potential temperature and salinity (Figures 3 and 4) suggest that diluted AABW is found below 5000 m depth in the northern and western section. Evidence for a large body of AABW due principally to vertical mixing with the overlaying NADW is seen in the dissolved oxygen distribution (Figure 6) at the northwestern corner of the hydrographic box. AABW flows into the Canary Basin through the Vema Fracture Zone at 11°N [*McCartney et al.*, 1991].

4. Geostrophic Transport

[13] The neutral density level 28.072 kg m^{-3} is used as the reference level of no motion to integrate the thermal

Table 1. Layer Definitions and Approximate Equivalences With Water Masses

Layer	Lower Interface γ_n, kg m^{-3}	Water Wass
1	26.44	surface water
2	26.85	NACW/SACW
3	27.162	NACW/SACW
4	27.38	NACW/SACW
5	27.62	MW/AAIW
6	27.82	MW/AAIW
7	27.922	MW/AAIW
8	27.975	UNADW
9	28.008	MNADW
10	28.044	MNADW
11	28.072	MNADW
12	28.0986	LNADW
13	28.11	LNADW
14	bottom	diluted AABW

wind equation. This level generally occurs at the 3000 m isobath, along the interface separating MNADW and LNADW (Figure 5, dashed line). If one or both stations of each station pair is shallower than 28.072, the deepest common level is used as the reference level. In neighboring stations with different bottom depths the velocity below the greatest common depth is considered constant and equal to the deepest value. Bathymetry from the *Smith and Sandwell* [1997] database is used between stations to compute geostrophic transport rather than bathymetry in each station. The choice of the reference level of no motion at γ_n = 28.072 kg m^{-3} follows the study of *Ganachaud* [2003a] for the North Atlantic. Studies carried out in the North Atlantic Subtropical Gyre transoceanic section at 24°N chose a pressure constant reference level at 3200 db in the eastern basin [*Lavín et al.*, 2003; *Rosón et al.*, 2003]. They later added a small barotropic velocity to balance the mid-ocean geostrophic and Ekman mass transports with the Florida Straits transport. *Roemmich and Wunsch* [1985] used an initial reference level of σ_2 = 36.8 (approximately 1300 m depth) and also added a small barotropic velocity. They pointed out that changes in the reference surface do not greatly affect the results.

[14] The water column is divided into a number of layers based on the neutral density that roughly separates different water masses (Figure 5). Table 1 shows the layer definitions and approximate equivalences with water masses. These layers are identical to those used by *Ganachaud* [2003a] for the North Atlantic. The upper four layers coincide with the thermocline waters, the next three ones (27.38 < γ_n < 27.922 kg m^{-3}) with intermediate waters, and the lowest layers with the different water masses of the NADW and the AABW. Ekman transport has been added to the shallowest layer. It has been computed across every section from remotely sensed estimates by the Active Microwave Instrument (AMI) on board the ERS-2 satellite for the period January–December 2003. Those data with a spatial resolution of 1° are scaled to 10 m height. Initially, Ekman transport for the north, west and south sections are 0.5, −0.9 and 1.0 Sv, respectively. As we will see the inverse model adjusts these values to the specific oceanographic conditions at the time of our survey.

[15] Figure 7 shows the integrated mass and anomalies of salt and heat transport in each section using the initial level at 28.072 kg m^{-3} for geostrophy and adding the Ekman transport in the first layer. The property anomalies are obtained by subtracting the mean property value. In the thermocline layers (layers 1–4), a main net southward and westward flow is clearly observed. Mass transport at intermediate (5–7) and upper deep (8–12) layers is low and increases at the two deepest layers. Figure 7 shows that the initial reference layer brings a certain imbalance at the thermocline and deepest layers. The adjustment is done applying a box inverse model.

5. Inverse Box Model Calculations

5.1. Model

[16] *Wunsch* [1978] was the first to describe the inverse box model applied to hydrographic data within a box. It provides a simple efficient method to obtain the geostrophic flow that obeys conservation statements for different properties in a volume of ocean bounded by hydrographic sections and land in the horizontal and neutral density layers in the vertical. The inverse box model assumes a time independence of the data which means that the time scale variability of the flow field is larger than the duration of the CORICA cruise [*Fu*, 1981; *Roemmich and Wunsch*, 1985]. The inverse box model provides an estimate of the velocities in the premise reference level of no motion along with their error covariance. In this study, we have extended the inverse model formulated by *Joyce et al.* [2001] to include the approximate conservation of mass and anomalies of salinity and heat, and to allow the transfer of properties between layers [*Macdonald*, 1998; *Sloyan and Rintoul*, 2000; *Ganachaud*, 2003a]. The following equations have to be solved:

$$\int\int \rho b dx dz + A_z \times (w^* \overline{\rho}) = -\int\int \rho v_r dx dz + Q \qquad (1)$$

$$\int\int \rho(C-\overline{C}) b dx dz + A_z \times \left(w^* \overline{\rho(C_i - C)} - \kappa^* \overline{\frac{\partial(\rho C)}{\partial z}} \right) = -\int\int \rho(C-\overline{C}) v_r dx dz + \overline{C} \times Q \qquad (2)$$

Equation 1 is used for mass and equation 2 for property anomalies. The first and last integral terms are derived from the reference velocities (b) and the relative velocity (v_r), respectively. The second term relates to the vertical transfer for each layer (w^* and κ^* represent the equivalent average dianeutral velocity and diffusivity across the interfaces, respectively) and Q takes into account the possible source or sink for any property including freshwater flux and Ekman flux. The horizontal average property and property gradient on a neutral density are computed from the bounding sections. x and z are the horizontal and vertical coordinates, respectively, A_z is the horizontal area of a given neutral surface bounded by the three sections and the African coast computed from temperature and salinity values from *Levitus and Boyer* [1994] and *Levitus et al.* [1994], and ρ, C, $\overline{C}$ and $\overline{C_i}$ are the density, the property concentration per unit of mass, the mean in each layer and the mean in every interface, respectively. The use of property anomalies improves the conditioning of the inverse problem resulting

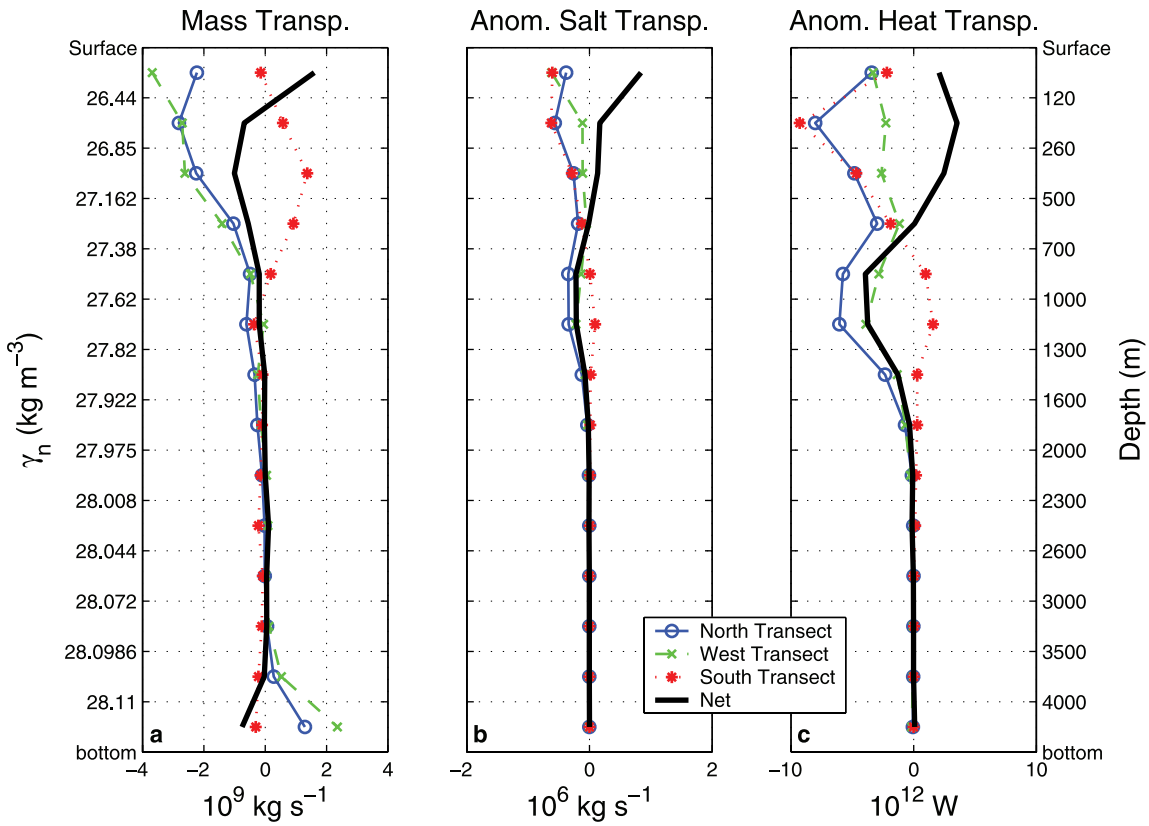

Figure 7. (a) Integrated mass, (b) anomaly salt, and (c) anomaly heat transports as a function of density layer for the north (circles, thin solid line), west (crosses, dashed line), and south (stars, dotted line) sections together with their sum (thick solid line). For each section, positive/negative sign means northward/southward or eastward/westward flow. The sign of the net transport is taken positive/negative for divergence/convergence flow out/in the box.

in a higher rank set of equations [*McIntosh and Rintoul*, 1997; *Ganachaud*, 2003b].

[17] If we consider equations for conservation of mass and salinity anomalies for each layer, and the total, and heat anomalies for deep layers, they form the following matrix equation:

$$Ax + n = -\Gamma \tag{3}$$

where A is a matrix of known quantities, n is a column vector, whose elements are the noise of each equation, Γ is a vector representing the amount by which properties or anomalies of properties are initially imbalanced in each layer, and x is the column vector containing the unknown of the system:

$$\begin{pmatrix} (b_i)_{i=1,\ldots,N_{pair}} \\ (w_k^*)_{k=1,\ldots,M_{layer}-1} \\ (\kappa_k^*)_{k=1,\ldots,M_{layer}-1} \\ \Delta T_{Ek} \\ F_w \end{pmatrix}$$

N_{pair} is the number of station pairs; M_{layer} is the number of layers; ΔT_{Ek} is the adjustment of the Ekman transport and F_w is the freshwater flux that are solved as part of the inversion. Same w^* and κ^* are used for all properties. For a more detailed discussion of (3), see *Ganachaud* [1999, 2003b].

[18] The inverse problem consists of 103 unknowns and 37 equations comprising near conservation of mass and salinity anomaly for individual layers and overall, and heat anomaly for each deep layer. We have used Gauss-Markov estimates to solve the underestimated set of equations which produce a minimum error variance solution. Gauss-Markov needs an initial estimate of the unknowns to guide the model solution [*Wunsch*, 1996]. The preliminary variances assigned to the unknowns are $(0.02\ \mathrm{m\ s^{-1}})^2$ for the reference velocities for station pairs over the open ocean, and $(0.05\ \mathrm{m\ s^{-1}})^2$ over shallow waters close to the African coast, half of the estimate values for Ekman transport and freshwater flux obtained from SMD94 (Surface Marine Data, 1994) and WOA94 (World Ocean Atlas, 1994) climatological data [*da Silva and Levitus*, 1994], $(10^{-6}\ \mathrm{m\ s^{-1}})^2$ for the average dianeutral velocity, and $(10^{-4}\ \mathrm{m^2\ s^{-1}})^2$ for the average dianeutral diffusivity [*Toole and Warren*, 1993; *Robins and Bryden*, 1994; *Polzin et al.*, 1997; *Ganachaud*, 2003b]. No positive requirement is set for the average dianeutral diffusivity.

[19] For the a priori variance for each constraint the study of *Ganachaud* [2003b] states that the most dominant uncertainty in the conservation equations arise from the deviation of the baroclinic mass transport, at the time of the cruise, from their mean value. Previous studies of the Canary Current through the Canary Islands suggest a relatively high variability of the same order of magnitude as the mean flow.

Table 2. A Priori Uncertainties for the Conservation Equations of Mass[a]

Layer	Mass	S (Mean ± SD)	θ (Mean ± SD), °C
1	1.5	36.693 ± **0.364**	21.900 ± 0.694
2	1.5	36.176 ± **0.242**	16.057 ± 0.835
3	1.5	35.736 ± **0.140**	13.026 ± 0.541
4	1.5	35.438 ± **0.146**	10.505 ± 0.623
5	1	35.255 ± **0.216**	8.319 ± 0.973
6	1	35.259 ± **0.208**	6.856 ± 0.972
7	1	35.209 ± **0.146**	5.466 ± 0.710
8	0.5	35.109 ± **0.084**	4.347 ± **0.419**
9	0.5	35.044 ± **0.046**	3.676 ± **0.234**
10	0.5	34.995 ± **0.022**	3.153 ± **0.109**
11	0.5	34.958 ± **0.009**	2.721 ± **0.041**
12	0.5	34.926 ± **0.002**	2.358 ± **0.015**
13	0.5	34.905 ± **0.002**	2.127 ± **0.019**
14	0.5	34.892 ± **0.001**	1.986 ± **0.016**
Overall	4	35.193 ± **0.436**	5.726 ± 4.803

[a]Mean and standard deviation of salinity and potential temperature used to compute the a priori uncertainties for anomaly conservation equations of salinity and heat, respectively, are shown in bold.

Hernández-Guerra et al. [2002] using expandable bathythermograph sections, from Gran Canaria Island to the African coast for 2 years every 2 months show that the easternmost branch of the Canary Current deviates on the order of 1.4 Sv from the mean flow. *Hernández-Guerra et al.* [2003], using a 4-year current mooring in the Lanzarote passage, find that the deviation of the Canary Current is 1.1 Sv. With current meters installed at the intermediate layer, they also find that the variability at this level is 0.4 Sv. If we extend these results to the CORICA box we would chose higher values in the thermocline than in deep layers as by *Joyce et al.* [2001], but the highest value would be constrained as suggested by *Ganachaud* [2003b]. We selected values of $(1.5\ \mathrm{Sv})^2$ for the first four layers, $(1\ \mathrm{Sv})^2$ for the intermediate layers, $(0.5\ \mathrm{Sv})^2$ for the deep layers and $(4\ \mathrm{Sv})^2$ for the overall equation. The a priori uncertainties for salinity and heat anomaly constraints are estimated as fourfold, the product of the a priori variance in mass conservation and the standard deviation of properties within the relevant layer as proposed by *Ganachaud and Wunsch* [2003]. Table 2 summarizes the a priori uncertainty in the mass conservation equations per layer as well as the mean and standard deviation of the potential temperature and salinity used to compute the a priori uncertainty of the heat and salinity anomaly conservation equations. To study the sensitivity of the Gauss-Markov estimates, we compute the model resolution matrix [*Menke*, 1989]. It shows that the mass equations for each layer and overall, the salt anomaly equations for the five deepest layer and the heat anomaly equations are well resolved. The remaining equations are only partially resolved. We have tried with different a priori variances [*Vaniceck and Siedler*, 2002] and the results are not significantly different than ours.

5.2. Results

[20] Velocities with error bars for the reference layer as a function of the station pair determined by the inverse calculations are shown in Figure 8a. Values are uniformly very low (<1 cm s^{-1}). Uncertainties of every b_i are almost unchanged from the a priori values as in other inverse solutions [*Ganachaud et al.*, 2000; *Joyce et al.*, 2001]. The dianeutral velocities in the first two layers are negative although not significantly different from zero (Figure 8b). Downwelling of thermocline waters corresponds to the Ekman pumping in the subtropical gyres. The highest dianeutral velocities occurring at the bottom layer are consistent with AABW northward increases. Figure 8c shows that dianeutral diffusivities in the water column are very weak and indistinguishable from zero as observed in the interior ocean above smooth topography [*Polzin et al.*, 1997].

[21] The Ekman transport adjustment is -0.2 ± 0.3 Sv, 0.8 ± 0.4 Sv and -1.1 ± 0.3 Sv for the north, west and south sections, respectively. This results in an Ekman transport of 0.3 ± 0.3 Sv, -0.1 ± 0.4 Sv and -0.1 ± 0.3 Sv for each section that are added to the shallowest layer. Freshwater divergence that is computed as part of the solution of the inverse model is indistinguishable from zero, $(0.8 \pm 1.9)\times 10^{-2}$ Sv, and less than that from the *da Silva and Levitus* [1994] climatology that gives a net evaporation 3.8×10^{-2} Sv in the region.

[22] We have also computed the net heat exchange across our sections from the inverse results: 4.6×10^{-3} PW (1PW = 10^{15} W) with a very high uncertainty (39.2×10^{-3} PW). This corresponds to 3.8 ± 32.4 W m^{-2} integrated over the oceanic region bounded by the hydrographic sections and the African coast. The annual mean oceanic heat gain from the *da Silva and Levitus* [1994] climatology data integrated over the same region is 31.9 W m^{-2}.

[23] We used the results from the inverse calculations to compute new integrated mass transport per density layer (Figure 9). Net mass imbalance is 0.04 ± 0.67 Sv. Mass imbalance in every layer is smaller than 0.5 Sv and indistinguishable from zero except for the first layer which is 1.1 ± 1.0 Sv. The comparison of Figures 7 and 9 shows an improvement in the mass conservation for each layer especially in the thermocline and bottom layers.

[24] A second shallower reference layer at $\gamma_n = 28.072$ kg m^{-3} was used to check if the inverse box model solutions converged. Reference, dianeutral velocities, and dianeutral diffusivities were indistinguishable in both reference layers. Mass transports in the surface and intermediate layers were also not significantly different. Deep mass transport for the shallower layer was higher than for the deeper layer. It yields a stream function that does not match the oxygen distribution.

6. Adjusted Mass Transport

[25] Figure 10 shows the integrated mass transport stream functions for different groups of layers corresponding to the thermocline (1–4), intermediate (5–7) and deep (8–14) layers. A surprising pattern, observed in the thermocline and intermediate accumulated transport, is the existence of mesoscale eddy features north of the Canary Islands resulting a saw-like stream functions. Although the existence of mesoscale eddies south of the Canary Islands due to the Von Karman street phenomena is well described [*Arístegui et al.*, 1994, 1997; *Sangrà et al.*, 2005], this is the first time that these structures have been seen in the north. These structures do not have an obvious explanation and it is not possible to explain them under the Von Karman dynamics. As observed in Figure 10, the pattern of circulation for these layers are different and will be described separately.

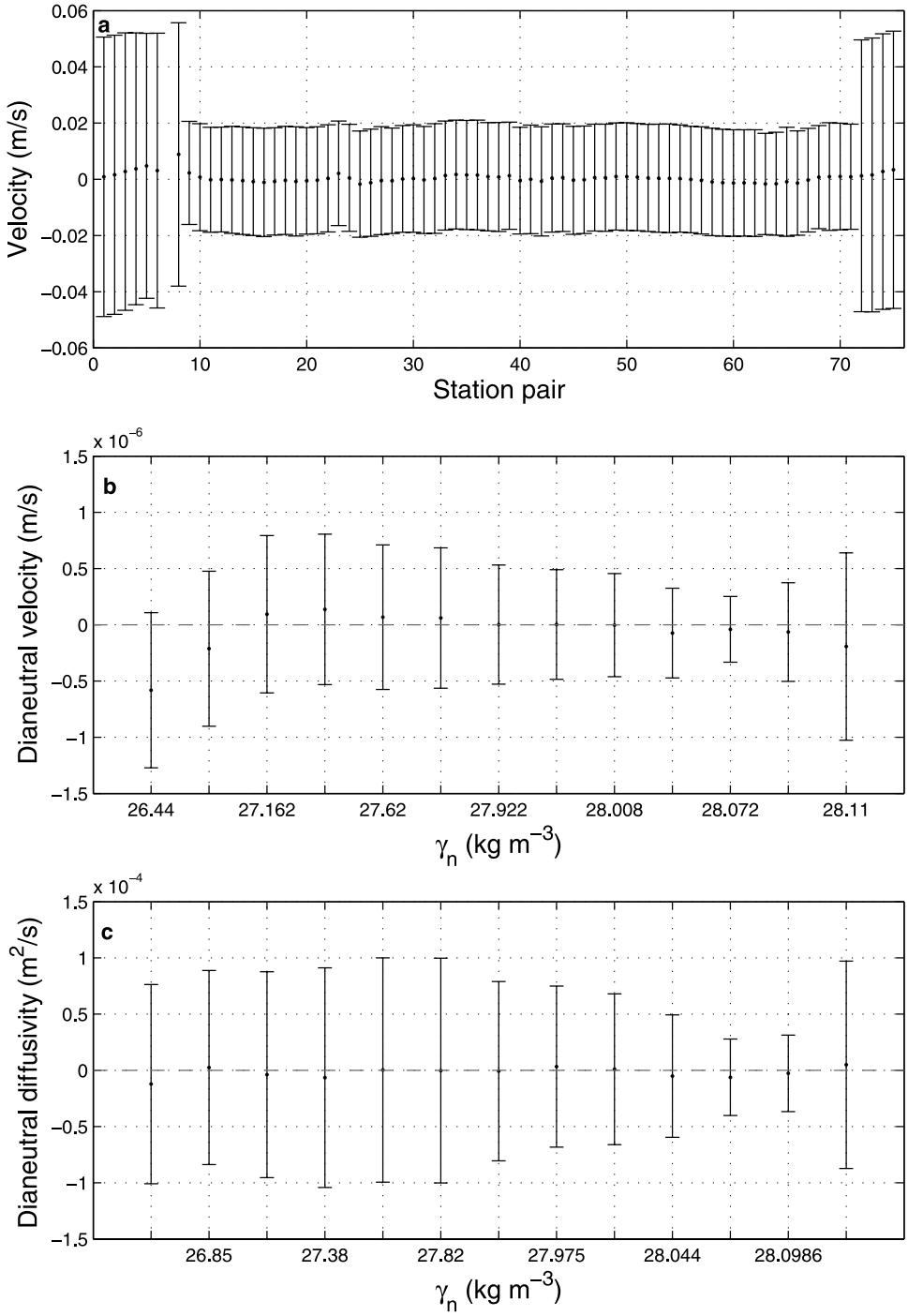

Figure 8. a) Velocity values for each station pair, (b) dianeutral velocities, and (c) dianeutral diffusivities between layers determined by inverse calculations together with the error bars.

[26] The thermocline layer shows a northward flow of 1.1 ± 0.5 Sv between Lanzarote and the African coast in the so-called Lanzarote passage as observed previously in autumn [*Hernández-Guerra et al.*, 2003]. Southward flow starts west of Lanzarote suggesting a westward displacement of the Canary Current in autumn as described by Machín et al. (submitted manuscript, 2005). From here, a southward flow of 5.8 ± 0.6 Sv transporting NACW is seen to 19°W. From the African coast, the net southward flow of the Canary Current is 4.7 ± 0.8 Sv. Through the Canary Islands, the Canary Current transports 4.0 ± 0.7 Sv. These results cannot be compared directly with those of *Stramma* [1984] because of differences in the definition of the thermocline layer. *Stramma* [1984] ascribes thermocline layer to a constant 800 m over the region. However, he is in agreement with us that the Canary Current flows southward at a rate of approximately 4 Sv. A surface manifestation of the meddy, transporting anticyclonically 4.1 ± 0.5/3.2 ± 0.5 Sv, is clearly observed between 19°W and 21°W. Between west of the meddy and about 24.5°W, there

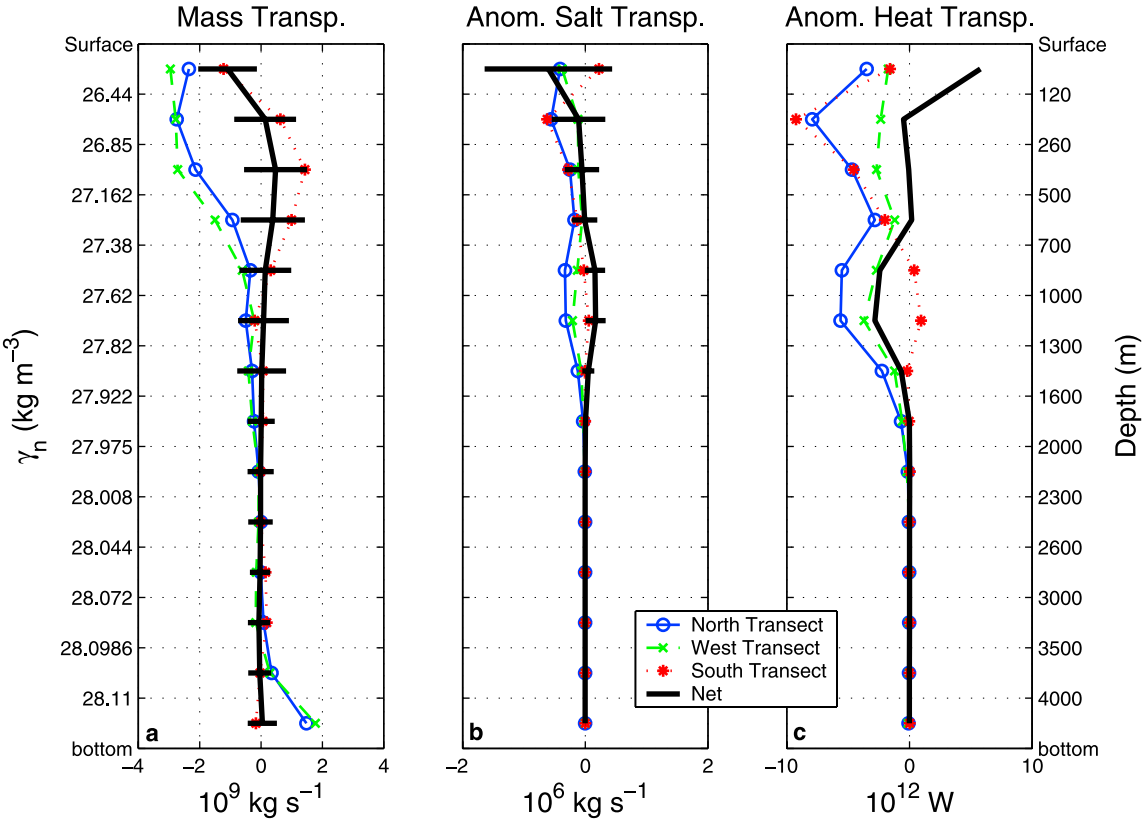

Figure 9. As in Figure 7 but using the solution of the inverse model.

is a weak circulation transporting 2.2 ± 0.7 Sv of NACW to the north. West of 24.5°W, the stream function oscillates between southward flow to the end of the northern section and westward flow to about 28°N in the western section. We might ascribe these two regimes of flow to a large anticyclonic mesoscale eddy, with a radius of roughly 150 km transporting 4.8 ± 0.6/5.4 ± 0.6 Sv. However, *Stramma* [1984] considers this flow to be a branch of the Azores Current flowing southward. He finds transports of 5 Sv in a wider latitude/longitude range than us: 20°–26°W at the norther section and 26°–29°N at the western section. South of the eddy, an eastward circulation of 1.0 ± 0.8 Sv is seen at roughly 26°N that matches the northward flow in the northern section. This is a region of relatively "pure" NACW that is transported to the north. From 26°N to about 20°N, the Canary Current feeds the North Equatorial Current which transports a mixture of NACW and SACW to the west at a rate of 5.5 ± 0.7 Sv. The thermocline stream function in the southern section oscillates north-south indicating the meandering of the CVFZ. The net northward transport in the southern section is 1.8 ± 0.6 Sv. This flow carries the SACW to northern latitudes and presumably forms a second front between NACW and SACW.

[27] The stream function at the intermediate layer shows a very weak and not significantly different than zero transport of 0.2 ± 0.9 Sv in the southern section. In the northwestern section, the flow is southwestward at a rate of 1.1 ± 1.1/1.2 ± 1.1 Sv. Although these flows are relatively weak and very uncertain, they carry MW to the ocean interior. In the northern transect, the anticyclonic meddy transports high-salinity water at a rate of approximately 2.6 ± 0.7 Sv. The northward transport of low-salinity water east of Lanzarote Passage is 0.7 ± 0.5 Sv as previously measured [*Hernández-Guerra et al.*, 2003].

[28] Mass transport in the deep layer is relatively weak. We will focus on the circulation in the extreme oxygen distribution below γ_n = 28.0986 kg m^{-3}. The relative oxygen minimum is observed east of 18°W and 23°W in the northern and southern sections, respectively, where the bathymetry is shallower than 4000 m depth. Mass transports are essentially zero −0.1 ± 0.4 Sv and 0.1 ± 0.7 Sv, respectively supporting the premise that this water has not been ventilated recently. The relative oxygen maximum distribution is found at the northwestern corner of the box. Figure 10 suggests that relatively younger waters are transported northeastward by a northward flow of 2.3 ± 2.4 Sv, west of 23°W in the northern section, and by an eastward flow of 2.1 ± 3.2 Sv, north of 24°N in the western section.

7. Discussion

[29] The Canary Current flows southward at a rate of 4.7 ± 0.8 Sv at the latitude of the Canary Islands, from the African coast to 19°W. This net flow is divided into a northward circulation of 1.1 ± 0.5 Sv between the African coast and Lanzarote Island and a southward circulation of 5.8 ± 0.6 Sv, similar to that obtained by *Paillet and Mercier* [1997] from an inverse model using historical hydrographic data. The Canary Current transports pure NACW southward. The North Equatorial Current transports a mixture of NACW and SACW as a result of the northward advection of SACW

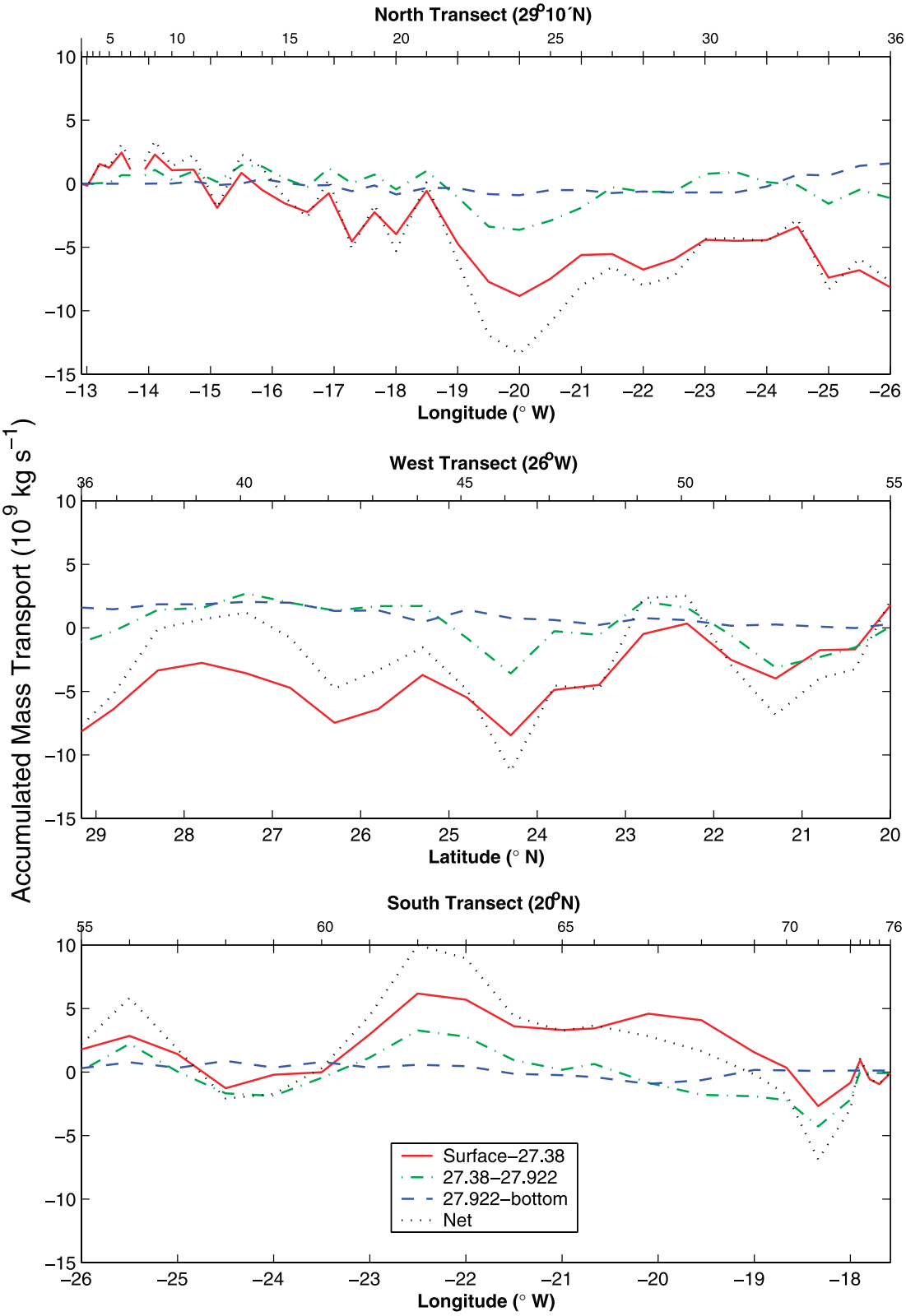

Figure 10. Integrated mass transport stream functions for different groups of layers corresponding to the thermocline (layers 1–4, $\gamma_n < 27.38$), intermediate (layers 5–7, $27.38 < \gamma_n < 27.922$), and deep (layers 8–14, $\gamma_n > 27.922$) as the result of the inverse model. The integration begins at the coast of Africa close to the Canary Islands. Positive/negative accumulated mass transport is taken for divergence/convergence flow out/in the box. The gap in the stream function in Figure 10 (top) is at Lanzarote island. Top axes show the CTD station position.

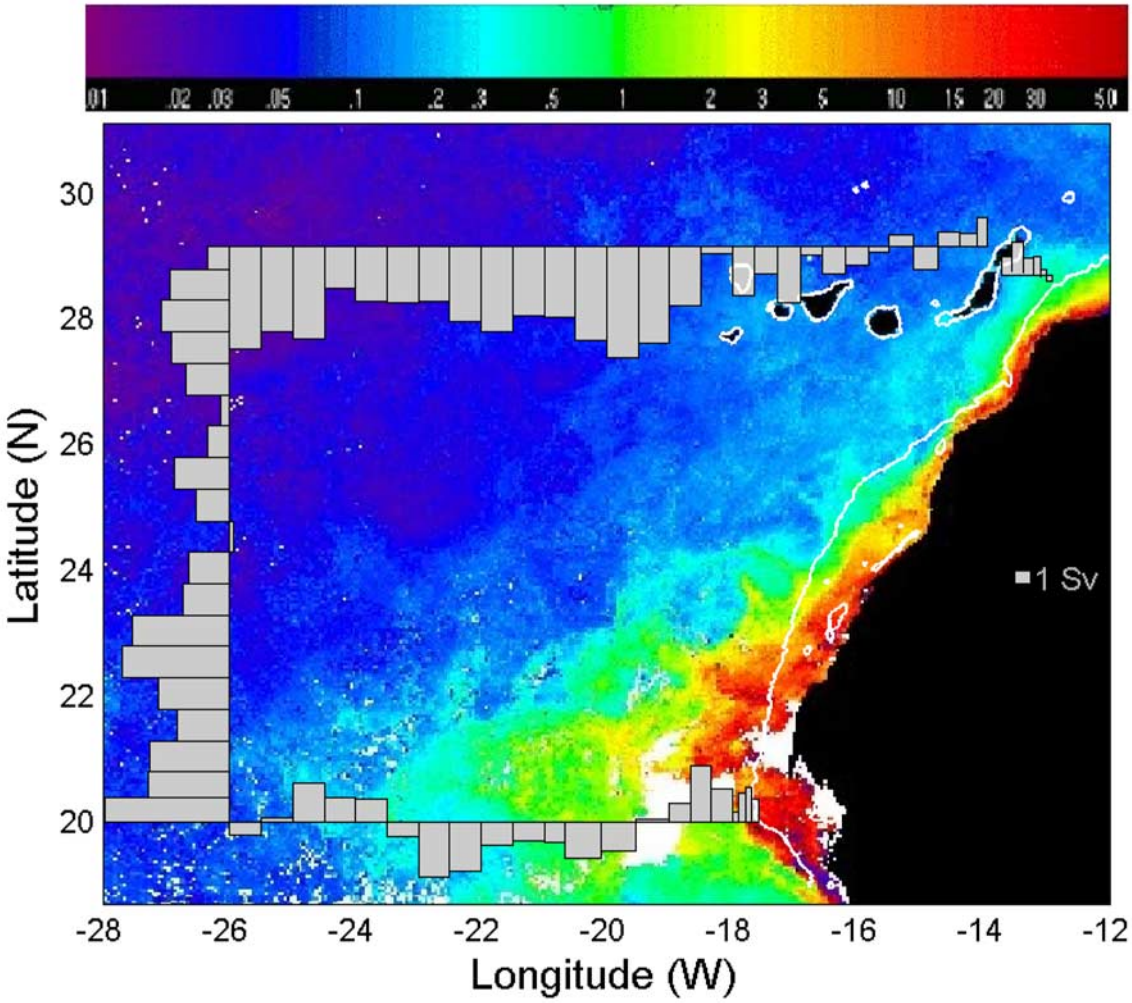

Figure 11. Image of phytoplankton pigment concentration from SeaWifs data corresponding to September 2003 monthly mean together with the accumulated mass transport for the surface layer. Land and clouds are represented in black and white, respectively. The color bar indicates the phytoplankton pigment concentration (in mg m^{-3}) of every pixel in the image. The white curve along the African coast is the 200 m isobath.

well beyond the Cape Verde Frontal Zone, and forms a second front as previously pointed out by *Arhan et al.* [1994]. Along the sections, several eddies intersect, some of them as energetic as the Canary Current. Eddies south of the Canary Islands are easily observed in satellite images [*Barton et al.*, 2004]. In the CORICA cruise, a set of eddies are seen north of the Canary Islands transporting as much as 3.8 ± 0.3 Sv and 1.2 ± 0.4 Sv at the thermocline and intermediate layers, respectively.

[30] Figure 11 shows phytoplankton pigment concentration, corresponding to the September 2003 monthly mean, together with the integrated mass transport for the surface layer. The phytoplankton pigment concentration image was created using all of the available SeaWifs data in September 2003. The daily images are overlayed on each other and a new image is created, which at each pixel retains the mean phytoplankton pigment concentration. The initial spatial resolution of SeaWifs data is reduced to 5 km in order to visualize the large-scale pattern. Upwelled waters with the highest pigment concentration are located along the African coast inshore of the shelf except for the giant filament off Cape Blanc [*Gabric et al.*, 1993]. As seen in Figure 11, upwelled waters with a relatively high phytoplankton pigment concentration extend offshore beyond the edge of the eastern boundary of the Canary Current due to the interaction between eddies generated downstream of the islands and the upwelling filaments as pointed out by *Barton et al.* [2004]. Thus the Canary Current transports the organic matter from the upwelling system off northwest Africa southwestward, to the oligotrophic open ocean.

[31] In the intermediate layer, there exists an anticyclonic meddy, located at the northern section with a transport of a 2.6 ± 0.7 Sv, and a southwestward flow of 1.2 ± 1.1 Sv, both of which transport MW to the ocean interior. If we considerer as a typical southwestward velocity of a meddy in the Canary Basin 2.0 cm s^{-1} as suggested by *Richardson et al.* [2000], the southwestward salt flux transported by the meddy is 138.9 × 10^6 kg s^{-1}. However, the net flow only transports 44.1 ± 39.6 × 10^6 kg s^{-1} of salt southwestward. This result confirms the importance of meddies in main-

taining the Mediterranean salt tongue in the North Atlantic as suggested by *Richardson et al.* [1989] and *Mazé et al.* [1997].

[32] The mass transport is approximately zero except in the deepest layer in the areas deeper than 5000 m, which is in accordance with the flow statistics of a set of current meters installed in the region by *Müller and Siedler* [1992]. The current meters below 5000 m show a fluctuating part of energy per mass (FKE) higher than those at shallower depths as shown by Machín et al. (submitted manuscript, 2005). Oxygen distribution and mass transport suggest that a water mass colder than 2.2°C is transported northeastward and may be related to the northward flow of diluted AABW described by *McCartney et al.* [1991]. According to these authors, a modified AABW enters the Canary Basin through a gap at 38°W in the Cape Verde Ridge after spreading the AABW into the eastern basin of the North Atlantic through the Vema Fracture Zone at 11°N.

[33] *Polzin et al.* [1997] indicate that a very intense mixing over a broad depth range is supported under low stratification, vigorous flow and rough bathymetry conditions. Our area presents none of these conditions and the dianeutral diffusivities are not significantly different than zero. Dianeutral velocities are also not significantly different than zero.

[34] In the Southeastern North Atlantic Subtropical Gyre, the heat flux divergence is very weak and the uncertainty resulting from the inverse model makes it indistinguishable from zero. The heat transport across the sections resembles the thermocline circulation. The north and south sections transport southwestward a heat flux of 0.62 ± 0.06 PW and 0.67 ± 0.06 PW, respectively, and the south section transports northward a heat flux of 0.05 ± 0.04 PW. It is not surprising that a freshwater flux indistinguishable from zero is obtained, because it is statistically significant only when integrated over very large areas as stated by *Ganachaud and Wunsch* [2003].

[35] **Acknowledgments.** This work has been supported by the Ministerio de Eduación y Ciencia under the CORICA project (REN2001-2649-C02-01). We thank the officers and crew of the R.V. *Thalassa* for their help during the cruise and the IEO for facilitating her use. Special gratitude goes to Francisco Machín for his Matlab inverse model scripts and Jane Dunworth-Baker for her very valuable help with the English language. We also thank two anonymous reviewers for their comments on this manuscript that helped to improve it. CERSAT (Centre ERS d'Archivage et de Traitement-French ERS Processing and Archiving Facility) provided the wind field. SeaWifs data were acquired and processed by the satellite receiving station at the Universidad de Las Palmas de Gran Canaria (http://www.webs.ulpgc.es/gyroscopecanarias/).

References

Arhan, M., A. Colin de Vèrdiere, and L. Memery (1994), The eastern boundary of the subtropical North Atlantic, *J. Phys. Oceanogr.*, *24*, 1295–1316.

Arístegui, J., P. Sangrà, S. Hernández-León, M. Cantón, A. Hernández-Guerra, and J. Kerling (1994), Island-induced eddies in the Canary Islands, *Deep Sea Res., Part I*, *41*, 1509–1525.

Arístegui, J., P. Tett, A. Hernández-Guerra, G. Basterretxea, M. Montero, K. Wild, S. Hernández-León, M. Cantón, J. García-Braun, M. Pacheco, and E. Barton (1997), The influence of island-generated eddies on chlorophyll distribution: A study of mesoscale variation around Gran Canaria, *Deep Sea Res., Part I*, *44*, 71–96.

Barton, E. (1987), Meanders, eddies and intrusions in the thermohaline front off northwest Africa, *Oceanol. Acta*, *10*, 267–283.

Barton, E., et al. (1998), The transition zone of the Canary Current upwelling region, *Prog. Oceanogr.*, *41*, 455–504.

Barton, E., J. Arístegui, P. Tett, and E. Navarro Pérez (2004), Variability in the Canary Islands area of filament-eddy exchanges, *Prog. Oceanogr.*, *62*, 71–94.

Cox, M., and K. Bryan (1984), A numerical model of the ventilated thermocline, *J. Phys. Oceanogr.*, *14*, 674–687.

da Silva, A., and S. Levitus (1994), *Atlas of Marine Data 1994*, vol. 1, *Algorithms and Procedures*, 83 pp., NOAA, Silver Spring, Md.

Emery, W., and J. Meincke (1986), Global water masses: Summary and review, *Oceanol. Acta*, *9*, 383–391.

Fiekas, V., J. Elker, T. Müller, A. Aitsam, and W. Zenk (1992), A view of the Canary Basin thermocline circulation, *J. Geophys. Res.*, *97*, 12,495–12,510.

Fratantoni, D., and P. Richardson (1999), SOFAR float observations of an intermediate-depth Eastern Boundary Current and mesoscale variability in the eastern tropical Atlantic Ocean, *J. Phys. Oceanogr.*, *29*, 1265–1278.

Fu, L. (1981), The general circulation and meridional heat transport of the subtropical South Atlantic determined by inverse methods, *J. Phys. Oceanogr.*, *11*, 1171–1193.

Gabric, A., L. Garcia, L. V. Camp, L. Nykjaer, W. Eifler, and W. Schrimpf (1993), Offshore export of shelf production in the Cape Blanc (Mauritania) giant filament as derived from coastal zone color scanner imagery, *J. Geophys. Res.*, *98*, 4697–4712.

Ganachaud, A. (1999), Large scale oceanic circulation and fluxes of freshwater, heat, nutrient and oxygen, Ph.D. thesis, MIT-WHOI Joint Program, Cambridge, Mass.

Ganachaud, A. (2003a), Large-scale mass transports, water mass formation, and diffusivities estimated from World Ocean Circulation Experiment (WOCE) hydrographic data, *J. Geophys. Res.*, *108*(C7), 3213, doi:10.1029/2002JC001565.

Ganachaud, A. (2003b), Error budget of inverse box model: The North Atlantic, *J. Atmos. Oceanic Technol.*, *20*, 1641–1655.

Ganachaud, A., and C. Wunsch (2003), Large-scale ocean heat and freshwater transports during the World Ocean Circulation Experiment, *J. Clim.*, *16*, 696–705.

Ganachaud, A., C. Wunsch, J. Marotzke, and J. Toole (2000), The meridional overturning and large-scale circulation in the Indian Ocean, *J. Geophys. Res.*, *105*, 26,117–26,134.

Gould, W. (1985), Physical oceanography of the Azores Front, *Prog. Oceanogr.*, *14*, 167–190.

Harvey, J. (1982), θ-S relationships and water masses in the eastern North Atlantic, *Deep Sea Res.*, *29*, 1021–1033.

Hernández-Guerra, A., J. Arístegui, M. Cantón, and L. Nykjaer (1993), Phytoplankton pigment patterns in the Canary Islands area as determined by using CZCS data, *Int. J. Remote Sens.*, *14*, 1431–1437.

Hernández-Guerra, A., F. López-Laatzen, F. Machín, D. de Armas, and J. Pelegrí (2001), Water masses, circulation and transport in the Eastern Boundary Current of the Subtropical Gyre, *Sci. Mar.*, *65*, 177–186.

Hernández-Guerra, A., et al. (2002), Temporal variability of mass transport in the Canary Current, *Deep Sea Res., Part II*, *19*, 3415–3426.

Hernández-Guerra, A., E. Fraile-Nuez, R. Borges, F. López-Laatzen, P. Vélez-Belcí, G. Parrila, and T. Müller (2003), Transport variability in the Lanzarote passage (Eastern Boundary Current of the North Atlantic Subtropical Gyre), *Deep Sea Res., Part I*, *50*, 189–200.

Iorga, M., and M. Lozier (1999), Signatures of the Mediterranean outflow from a North Atlantic climatology: 2. Diagnostic velocity fields, *J. Geophys. Res.*, *104*, 25,958–26,009.

Jackett, D., and T. McDougall (1997), A neutral density variable for the world's ocean, *J. Phys. Oceanogr.*, *27*, 237–263.

Joyce, T., A. Hernández-Guerra, and W. Smethie (2001), Zonal circulation in the NW Atlantic and Caribbean from a meridional WOCE hydrographic section at 66°W, *J. Geophys. Res.*, *106*, 22,095–22,113.

Käse, R., and G. Siedler (1982), Meandering of the subtropical front southeast of the Azores Current, *Nature*, *300*, 245–246.

Käse, R., J. Price, P. Richardson, and W. Zenk (1986), A quasi-synoptic survey of the thermocline circulation and water mass distribution within the Canary Basin, *J. Geophys. Res.*, *91*, 9739–9748.

Klein, B., and G. Siedler (1989), On the origin of the Azores Current, *J. Geophys. Res.*, *94*, 6159–6168.

Knoll, M., A. Hernández-Guerra, B. Lenz, F. López-Laatzen, F. Machín, T. Müller, and G. Siedler (2002), The Eastern Boundary Current system between the Canary Islands and the African coast, *Deep Sea Res., Part II*, *19*, 3427–3440.

Lavín, A., H. Bryden, and G. Parrilla (2003), Mechanisms of heat, freshwater, oxygen and nutrient transports and budgets at 24.5° n in the subtropical North Atlantic, *Deep Sea Res., Part I*, *50*, 1099–1128.

Levitus, S., and T. Boyer (1994), *World Ocean Atlas 1994*, vol. 4, *Temperature, NOAA Atlas NESDIS 4*, 129 pp., NOAA, Silver Spring, Md.

Levitus, S., R. Burgett, and T. Boyer (1994), *World Ocean Atlas 1994*, vol. 3, *Salinity, NOAA Atlas NESDIS 3*, 99 pp., NOAA, Silver Spring, Md.

Luyten, J., J. Pedlosky, and H. Stommel (1983), The ventilated thermocline, *J. Phys. Oceanogr.*, *13*, 292–309.
Macdonald, A. (1998), The global ocean circulation: A hydrographic estimate and regional analysis, *Prog. Oceanogr.*, *41*, 281–382.
Mazé, J., M. Arhan, and H. Mercier (1997), Volume budget of the eastern boundary layer off the Iberian Peninsula, *Deep Sea Res., Part I*, *44*, 1543–1574.
McCartney, M., S. Bennet, and M. Woodgate-Jones (1991), Eastward flow through the Mid-Atlantic Ridge at 11°N and its influence in the abyss of the Eastern Basin, *J. Phys. Oceanogr.*, *21*, 1089–1121.
McIntosh, P., and S. Rintoul (1997), Do box inverse models work?, *J. Phys. Oceanogr.*, *27*, 291–308.
Menke, W. (1989), *Geophysical Data Analysis: Discrete Inverse Theory*, *Int. Geophys. Ser.*, vol. 45, 289 pp., Elsevier, New York.
Müller, T., and G. Siedler (1992), Multi-year current time series in the eastern North Atlantic Ocean, *J. Mar. Res.*, *50*, 63–98.
Nykjaer, L., and L. Van Camp (1994), Seasonal and interannual variability of coastal upwelling along northwest Africa and Portugal from 1981 to 1991, *J. Geophys. Res.*, *99*, 14,197–14,207.
Pacheco, M., and A. Hernández-Guerra (1999), Seasonal variability of recurrent phytoplankton pigment patterns in the Canary Islands area, *Int. J. Remote Sens.*, *7*, 1405–1418.
Paillet, J., and H. Mercier (1997), An inverse model of the eastern North Atlantic general circulation and thermocline ventilation, *Deep Sea Res., Part I*, *44*, 1293–1328.
Parrilla, G., S. Neuer, P.-Y. Le Traon, and E. Fernández-Suárez (2002), Topical studies in oceanography: Canary Islands Azores Gibraltar observarions (CANIGO). I: Studies in the northern Canary Islands basin, *Deep Sea Res., Part II*, *49*, 3409–3413.
Pérez-Rodríguez, P., J. Pelegrí, and Marrero-Díaz (2001), Dynamical characteristics of the Cape Verde Frontal Zone, *Sci. Mar.*, *65*, suppl. 1, 241–250.
Polzin, K., J. Toole, G. Ledwell, and R. Schmitt (1997), Spatial variability of turbulent mixing in the abyssal ocean, *Science*, *276*, 93–96.
Richardson, P., S. Walsh, L. Armi, M. Schröder, and J. Price (1989), Tracking three meddies with SOFAR floats, *J. Phys. Oceanogr.*, *19*, 371–383.
Richardson, P., A. Bower, and W. Zenk (2000), A census of meddies tracked by floats, *Prog. Oceanogr.*, *45*, 209–250.
Robins, P., and H. Bryden (1994), Direct observations of advective nutrient and oxygen fluxes at 24°N in the Pacific Ocean, *Deep Sea Res., Part I*, *41*, 143–168.
Roemmich, D., and C. Wunsch (1985), Two transatlantic sections: Meridional circulation and heat flux in the subtropical North Atlantic Ocean, *Deep Sea Res.*, *32*, 619–664.
Rosón, G., A. Ríos, F. Pérez, A. Lavín, and H. Bryden (2003), Carbon distribution, fluxes, and budgets in the subtropical North Atlantic Ocean (24.5°N), *J. Geophys. Res.*, *108*(C5), 3144, doi:10.1029/1999JC000047.
Sangrà, P., J. Pelegrí, A. Hernández-Guerra, I. Arregui, J. Martín, A. Marrero-Díaz, A. Martínez, A. Ratsimandresy, and A. Rodríguez-Santana (2005), Life history of an anticylonic eddy, *J. Geophys. Res.*, *110*, C03021, doi:10.1029/2004JC002526.
Sloyan, B. M., and S. R. Rintoul (2000), Estimates of area-averaged diapycnal fluxes from basin-scale budgets, *J. Phys. Oceanogr.*, *30*, 2320–2341.
Smith, W., and D. Sandwell (1997), Global sea floor topography from satellite altimetry and ship depth soundings, *Science*, *277*, 1956–1962.
Speth, P., and H. Detlefsen (1982), Meteorological influences on upwelling off northwest Africa, in *The Canary Current: Studies of an Upwelling System*, *Rapp. Proc. Verbaux Réunions*, vol. 180, edited by G. Hempel, pp. 29–35, Cons. Int. pour L'Explor. de la Mer, Copenhagen.
Stramma, L. (1984), Geostrophic transport in the warm water sphere of the eastern subtropical North Atlantic, *J. Mar. Res.*, *42*, 537–558.
Stramma, L., and H. Isemer (1988), Seasonal variability of meridional temperature fluxes in the eastern North Atlantic Ocean, *J. Mar. Res.*, *46*, 281–299.
Stramma, L., and T. Müller (1989), Some observations of the Azores Current and the North Equatorial Current, *J. Geophys. Res.*, *94*, 3181–3186.
Stramma, L., and G. Siedler (1988), Seasonal changes in the North Atlantic Subtropical Gyre, *J. Geophys. Res.*, *93*, 8111–8118.
Sy, A. (1988), Investigation of large-scale circulation patterns in the central North Atlantic: The North Atlantic Current, the Azores Current, and the Mediterranean Water plume in the area of the Mid-Atlantic Ridge, *Deep Sea Res.*, *35*, 383–413.
Tomczak, M., and P. Hughes (1980), Three dimensional variability of water masses and currents in the Canary upwelling region, *Meteor Forschungsergeb. A*, *21*, 1–24.
Toole, J., and B. Warren (1993), A hydrographic section across the subtropical south Indian Ocean, *Deep Sea Res., Part I*, *40*, 1973–2019.
Tsuchiya, M., L. Talley, and M. McCarney (1992), An eastern Atlantic section from Iceland southward across the equator, *Deep Sea Res., Part I*, *39*, 1885–1917.
Van Camp, L., L. Nykjaer, E. Mittelstaedt, and P. Schlittenhardt (1991), Upwelling and boundary circulation off northwest Africa as depicted by infrared and visible satellite observations, *Prog. Oceanogr.*, *26*, 357–402.
Vaniceck, M., and G. Siedler (2002), Zonal fluxes in the deep water layers of the western South Atlantic, *J. Phys. Oceanogr.*, *32*, 2205–2235.
Wooster, W., A. Bakun, and D. McLain (1976), The seasonal upwelling cycle along the Eastern Boundary of the North Atlantic, *J. Mar. Res.*, *34*, 131–141.
Worthington, L. (1976), *On the North Atlantic Circulation*, 110 pp., Johns Hopkins Univ. Press, Baltimore, Md.
Wunsch, C. (1978), The North Atlantic general circulation west of 50°W determined by inverse methods, *Rev. Gephys.*, *16*, 583–620.
Wunsch, C. (1996), *The Ocean Circulation Inverse Problem*, 442 pp., Cambrige Univ. Press, New York.
Wüst, G. (1935), Schichtung und Zirkulation des Atlantischen Ozeans: Die Stratosphare des Atlantischen Ozeans, in *Wissenschaftliche Ergebnisse der Deutschen Atlantischen Expedition auf dem Forschungs–und Vermessungsschiff Meteor 1925–1927*, vol. 6, pp. 109–288, de Gruyter, New York.
Zenk, W., B. Klein, and M. Schröder (1991), Cape Verde Frontal Zone, *Deep Sea Res.*, *38*, S505–S530.

E. Fraile-Nuez, A. Hernández-Guerra, and A. Martínez, Facultad de Ciencias del Mar, Universidad de Las Palmas de Gran Canaria, E-35017 Las Palmas, Spain. (ahernandez@dfis.ulpgc.es)
F. López-Laatzen and P. Vélez-Belchí, Centro Oceanográfico de Canarias, Instituto Español de Oceanografía, E-38080 Santa Cruz, Spain.
G. Parrilla, Intituto Español de Oceanografía, Corazón de María 8, E-28002 Madrid, Spain.